

Receiving amplitude-phase shift keying signals in microwave fields with a Rydberg atomic receiver

Zhida Wang(王志达), Yang Yan(燕阳), Xinyi Y. I. Xu(徐新异), Wei E. I. Sha(沙威), Xinyan Liang(梁新彦), Jinpeng Yuan(元晋鹏), Lirong Wang(汪丽蓉), Liantuan Xiao(肖连团), Suotang Jia(贾锁堂)

Citation: Chin. Phys. B. 35, 083203 (2026). DOI: 10.1088/1674-1056/ae37fb
http://cpb.iphy.ac.cn; http://iopscience.iop.org/cpb

What follows is a list of articles you may be interested in

Co-optimization of linear gain and dynamic range for atomic superheterodyne receivers based on homodyne readout

Chuan Qu(瞿川), Dongqin Guo(郭东琴), Jian Zhang(张剑)
Chin. Phys. B. 35, 013202 (2026). DOI: 10.1088/1674-1056/ade8e9

Optimization strategies for operational parameters of Rydberg atom-based amplitude modulation receiver

Yuhao Wu(吴宇豪), Dongping Xiao(肖冬萍), Huaiqing Zhang(张淮清), Sheng Yan(阎晟)
Chin. Phys. B. 34, 013201 (2025). DOI: 10.1088/1674-1056/ad886a

Spin-exchange relaxation of naturally abundant Rb in a K-Rb-^{21}Ne self-compensated atomic comagnetometer

Yan Lu(卢妍), Yueyang Zhai(翟跃阳), Yong Zhang(张勇), Wenfeng Fan(范文峰), Li Xing(邢力), Wei Quan(全伟)
Chin. Phys. B. 29, 043204 (2020). DOI: 10.1088/1674-1056/ab75d3

SPECIAL TOPIC — Quantum frontiers with Rydberg atoms

Receiving amplitude-phase shift keying signals in microwave fields with a Rydberg atomic receiver

Zhida Wang(王志达)[1,2], Yang Yan(燕阳)[1,2], Xinyi Y. I. Xu(徐新异)[3], Wei E. I. Sha(沙威)[3], Xinyan Liang(梁新彦)[4], Jinpeng Yuan(元晋鹏)[1,2,†], Lirong Wang(汪丽蓉)[1,2,‡], Liantuan Xiao(肖连团)[1,2], and Suotang Jia(贾锁堂)[1,2]

[1] *State Key Laboratory of Quantum Optics Technologies and Devices, Institute of Laser Spectroscopy, Shanxi University, Taiyuan* 030006, *China*
[2] *Collaborative Innovation Center of Extreme Optics, Shanxi University, Taiyuan* 030006, *China*
[3] *College of Information Science and Electronic Engineering, Zhejiang University, Hangzhou* 310027, *China*
[4] *Institute of Big Data Science and Industry, Shanxi University, Taiyuan* 030006, *China*

(Received 19 November 2025; revised manuscript received 6 January 2026; accepted manuscript online 14 January 2026)

The Rydberg atomic receiver (RAR), characterized by its broad bandwidth, high sensitivity, traceability, and all-optical readout, has substantial potential in wireless communication. We implement the reception of amplitude-phase shift keying (APSK) modulated microwave signals using the RAR, where its self-demodulation capability, based on electromagnetically induced transparency (EIT) and Autler–Townes (AT) splitting, preserves amplitude and phase information for decoding and data recovery. The relationship between amplitude and phase encoding orders in different APSK schemes and the bit error rate (BER) is explored. Relative to conventional amplitude-shift keying (ASK), APSK extends the phase dimension to increase data capacity proportional to the number of phase states. Additionally, APSK allows control of symbol durations, and the impact of varying symbol durations on data recovery is assessed through image transmission. This work utilizes the self-demodulation capabilities of the RAR to implement APSK within a quantum framework, thereby providing new insights for advancing quantum sensing and communication applications.

Keywords: Rydberg atomic receiver, self-demodulation, amplitude and phase-shift keying

PACS: 32.80.Ee, 42.50.Gy, 84.40.–x, 84.30.Qi

DOI: 10.1088/1674-1056/ae37fb **CSTR:** 32038.14.CPB.ae37fb

1. Introduction

Rydberg atoms inherently exhibit large susceptibility, large transition dipole moments, and strong interactions, conferring extraordinary sensitivity to external microwave signals.[1–5] The all-optical readout and broad bandwidth of Rydberg atom-based systems position them as ideal candidates for communication receivers in wireless communications.[6–12] A Rydberg atomic receiver (RAR) leverages its quantum coherent properties to perform operations such as down-conversion and filtering, enabling direct demodulation of modulated signals.[13,14]

Various modulation techniques based on RAR have been explored in the field of wireless communication.[15–17] In amplitude modulation (AM), RAR leverages electromagnetically induced transparency (EIT) and Autler–Townes (AT) splitting to achieve high-sensitivity signal reception from C-band to terahertz.[18–26] For frequency modulation (FM), their broadband tunability enables stable multi-channel audio signal reception, improving interference resilience in complex communication scenarios.[27–29] In phase modulation (PM), RAR optimizes signal resolution for frequency-division multiplexing communication through heterodyne detection, demonstrating potential for low error rates and robust noise resistance.[30,31] Rather than utilizing a single dimension of the signal for information bearing, higher-order modulation schemes can provide greater information capacity.[32–34] For instance, quadrature amplitude modulation (QAM) has been successfully demonstrated in RAR, verifying the capability of atomic systems to handle simultaneous amplitude and phase variations.[35] Amplitude-phase shift keying (APSK) is also a higher-order digital modulation technique that simultaneously encodes information in both amplitude and phase.[36,37] APSK offers greater flexibility in constellation mapping than QAM, thereby alleviating, to some extent, the sensitivity of rectangular constellations to amplitude noise.[38–40] However, APSK has yet to be employed in RAR, which would extend the existing higher-dimensional modulation schemes.

In this work, the reception of APSK signals modulated onto the microwave field is implemented via the RAR by exploiting its inherent self-demodulation capability. The mapping between binary codes and their corresponding amplitude and phase values for symbols is clearly depicted. Pseudo-

†Corresponding author. E-mail: yjp@sxu.edu.cn
‡Corresponding author. E-mail: wlr@sxu.edu.cn

© 2026 Chinese Physical Society and IOP Publishing Ltd. All rights, including for text and data mining, AI training, and similar technologies, are reserved.

random bit sequences were transmitted to validate the feasibility of the APSK method. The bit error rate (BER) of APSK signals with different encoding orders was evaluated, including separate BERs for amplitude and phase, along with a comparison of the information capacity of ASK. Additionally, a 33×33 pixel quick response (QR) code signal was sent to assess the influence of different symbol durations. This work addresses the absence of APSK-related research in RAR by realizing an APSK modulation scheme through the integration of a phase dimension into ASK, substantially improving its information capacity.

2. Experimental setup

The encoding process of the APSK signal is illustrated in Fig. 1(a). The bit sequence is divided into two groups and respectively mapped to amplitude and phase values. The number of bits in the sequence division and the number of mapped values are determined by the order of the APSK. The amplitude and phase values are encoded into the sine wave, where the unique waveform corresponding to each different combination of amplitude and phase represents a symbol, and the number of cycles occupied by the symbol is its duration. All symbols carrying the binary information are sequentially concatenated to form the payload section. The preamble and postamble segments are appended to the beginning and end of the payload to calibrate symbol duration, assist in signal triggering, and identify the complete signal.

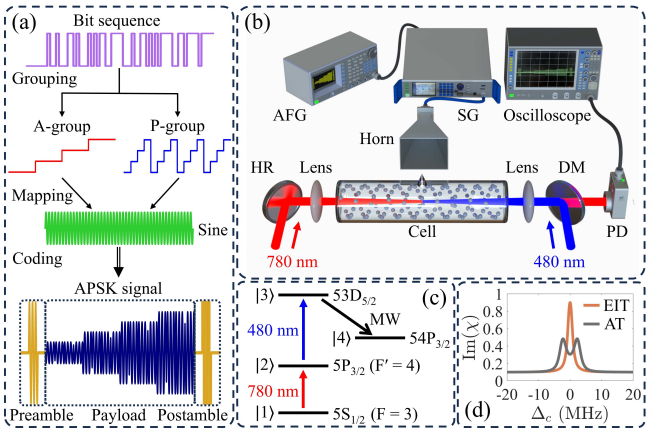


Fig. 1. (a) Schematic of the APSK signal encoding process. *A*-group, amplitude group; *P*-group, phase group. (b) Schematic of the experimental setup. HR, high-reflectivity mirror; Cell, atomic vapor cell; DM, dichroic mirror; PD, photodetector; Horn, horn antenna; AFG, arbitrary function generator; SG, signal generator. (c) Energy-level diagram of the ^{85}Rb atom used in the experiment. (d) Theoretical simulations of different energy-level configurations as a function of the coupling-laser frequency detuning.

The schematic diagram of the experimental configuration is presented in Fig. 1(b). The 780 nm probe laser, provided by an external cavity diode laser (DL pro, Toptica), is frequency-locked to the $5S_{1/2}$ $(F = 3) \rightarrow 5P_{3/2}$ $(F' = 4)$ hyperfine transition using saturation absorption spectroscopy. The 480 nm coupling laser, provided by a frequency-doubled amplified diode laser (DLC TA-SHG pro, Toptica), is frequency-locked to the $5P_{3/2}$ $(F' = 4) \rightarrow 53D_{5/2}$ transition. The probe and coupling beams counter-propagate through a 100 mm long, 25 mm diameter ^{85}Rb vapor cell with respective powers of 180 μW and 400 mW and beam diameters of 200 μm and 250 μm. The transmitted probe laser signal is detected by a photodetector (PDA36A, Thorlabs). The time-domain signal detected by the photodetector is recorded by an oscilloscope (RTO2004, Rohde & Schwarz). The APSK signal is imported into an arbitrary function generator (AFG3052C, Tektronix), which generates the signal at a frequency of 10 kHz. The signal is then modulated onto a 14.23 GHz microwave carrier, chosen to align with the operational frequency range of the experimental setup, using a signal generator (SMA100B, Rohde & Schwarz). The modulated microwave signal is transmitted through a horn antenna, and the distance between the horn antenna and the receiver is 1.30 m, satisfying the far-field condition. With insertion and propagation losses, the measured electric field strength at the receiver reaches 5.10 mV·cm^{-1}, corresponding to a dynamic range of 18 dB within the optimal linear response region at this detection distance. The system achieves an instantaneous bandwidth of approximately 100 kHz, which effectively ensures that the specific communication requirements are satisfied.

The relevant atomic energy levels employed in this experiment are depicted in Fig. 1(c). A weak 780 nm probe laser excites ^{85}Rb atoms from the ground state $5S_{1/2}$ $(F = 3)$ to the intermediate state $5P_{3/2}$ $(F' = 4)$, and a strong 480 nm coupling laser drives atoms from $5P_{3/2}$ $(F' = 4)$ to the Rydberg state $53D_{5/2}$. The 14.23 GHz millimeter-wave field is modulated by the APSK signal, thereby driving the transition between the Rydberg states $53D_{5/2}$ and $54P_{3/2}$.

The absorption of the probe laser is directly related to the imaginary part of the susceptibility $\mathrm{Im}(\chi)$, the variation of which as a function of the frequency detuning Δ_c of the coupling laser is illustrated in the theoretical simulations in Fig. 1(d). When the probe and coupling lasers interact with atoms in a three-level system, since part of the atomic population is trapped in the dark state, a transparent window appears in the absorption profile of the probe laser, which is the EIT shown by the orange line in Fig. 1(d). By introducing the microwave field, the system evolves into a four-level configuration, leading to the AT splitting indicated by the gray line in Fig. 1(d). The susceptibility is related to the coherence term ρ_{21} between $|2\rangle$ and $|1\rangle$. To accurately compute the steady-state solution of ρ_{21}, it is essential to employ the Hamiltonian, density matrix, and decoherence matrix of the four-level atomic system to construct the master equation. Under the rotating-wave and dipole approximations, the interaction Hamiltonian for the microwave-assisted four-level Ryd-

berg atomic system is given by

$$\boldsymbol{H} = \frac{\hbar}{2}\begin{pmatrix} 0 & \Omega_{\rm p} & 0 & 0 \\ \Omega_{\rm p} & -2\Delta_{\rm p} & \Omega_{\rm c} & 0 \\ 0 & \Omega_{\rm c} & -2(\Delta_{\rm p}+\Delta_{\rm c}) & \Omega_{\rm MW} \\ 0 & 0 & \Omega_{\rm MW} & -2(\Delta_{\rm p}+\Delta_{\rm c}+\Delta_{\rm MW}) \end{pmatrix}, \quad (1)$$

where $\hbar$ represents the reduced Planck constant, $\Delta_{\rm p}$, $\Delta_{\rm c}$, and $\Delta_{\rm MW}$ are the frequency detunings of the probe laser, coupling laser, and microwave field, respectively, defined as $\Delta_{\rm p} = \omega_{\rm p} - \omega_{12}$, $\Delta_{\rm c} = \omega_{\rm c} - \omega_{23}$, and $\Delta_{\rm MW} = \omega_{\rm MW} - \omega_{34}$. Here, $\omega_{\rm p}$, $\omega_{\rm c}$, and $\omega_{\rm MW}$ are the frequencies of the probe laser, coupling laser, and microwave field, respectively; ω_{12}, ω_{23}, and ω_{34} are the resonance frequencies of the $|1\rangle - |2\rangle$, $|2\rangle - |3\rangle$, and $|3\rangle - |4\rangle$ transitions, respectively. $\Omega_{\rm MW}$ is the Rabi frequency of the microwave field, defined as $\Omega_{\rm MW} = E_{\rm MW}\mu_{\rm MW}/\hbar$, where $E_{\rm MW}$ is the electric field strength of the microwave field, and $\mu_{\rm MW}$ is the transition dipole moment corresponding to the microwave field transition. For the four-level atomic system, the density matrix $\boldsymbol{\rho}$ has the following form:

$$\boldsymbol{\rho} = \begin{pmatrix} \rho_{11} & \rho_{12} & \rho_{13} & \rho_{14} \\ \rho_{21} & \rho_{22} & \rho_{23} & \rho_{24} \\ \rho_{31} & \rho_{32} & \rho_{33} & \rho_{34} \\ \rho_{41} & \rho_{42} & \rho_{43} & \rho_{44} \end{pmatrix}. \quad (2)$$

In the density matrix, the diagonal elements ρ_{ii} represent the atomic population probabilities of level $|i\rangle$, while the off-diagonal elements $\rho_{ij} = \rho_{ji}^*$ represent the coherence between levels $|i\rangle$ and $|j\rangle$. The time evolution of the density matrix is typically described using the Lindblad master equation. In general, the Lindblad master equation can be written as

$$\dot{\boldsymbol{\rho}} = -\frac{\rm i}{\hbar}[H,\rho] + \boldsymbol{L}(\rho), \quad (3)$$

where $[a,b] = ab - ba$ is the commutator, and $\boldsymbol{L}(\rho)$ is the Lindblad superoperator. In the four-level model considering only spontaneous emission, according to the transition selection rules, the decoherence matrix can ultimately be expressed as

$$\boldsymbol{L}(\rho) = \begin{pmatrix} \Gamma_2\rho_{22} & -\gamma_{12}\rho_{12} & -\gamma_{13}\rho_{13} & -\gamma_{14}\rho_{14} \\ -\gamma_{21}\rho_{21} & \Gamma_3\rho_{33} - \Gamma_2\rho_{22} & -\gamma_{23}\rho_{23} & -\gamma_{24}\rho_{24} \\ -\gamma_{31}\rho_{31} & -\gamma_{32}\rho_{32} & \Gamma_4\rho_{44} - \Gamma_3\rho_{33} & -\gamma_{34}\rho_{34} \\ -\gamma_{41}\rho_{41} & -\gamma_{42}\rho_{42} & -\gamma_{43}\rho_{43} & -\Gamma_4\rho_{44} \end{pmatrix}, \quad (4)$$

where $\gamma_{ij} = (\Gamma_i + \Gamma_j)/2$, where Γ_i and Γ_j are the decay rates of the atomic transitions. Under the initial and steady-state conditions ($\dot{\rho}_{ii} = \dot{\rho}_{ij} = 0$), the steady-state solution for the coherence term ρ_{21} in the four-level Rydberg atomic system is expressed as

$$\rho_{21} = \frac{{\rm i}\Omega_{\rm p}(4\gamma_{13}\gamma_{14} + \Omega_{\rm MW}^2)}{2(\gamma_{14}\Omega_{\rm c}^2 + \gamma_{12}\Omega_{\rm MW}^2 + 4\gamma_{12}\gamma_{13}\gamma_{14})}. \quad (5)$$

The susceptibility of the weak probe field, when $\Delta_{\rm p}$, $\Delta_{\rm c}$, and $\Delta_{\rm MW}$ are zero, is given by

$$\chi_{21} = \frac{{\rm i}N|\mu_{21}|^2(4\gamma_{13}\gamma_{14} + \Omega_{\rm MW}^2)}{2\varepsilon_0\hbar(\gamma_{14}\Omega_{\rm c}^2 + \gamma_{12}\Omega_{\rm MW}^2 + 4\gamma_{12}\gamma_{13}\gamma_{14})}, \quad (6)$$

where N represents the atomic number density, μ_{21} represents the transition dipole matrix element, and ε_0 represents the vacuum permittivity.

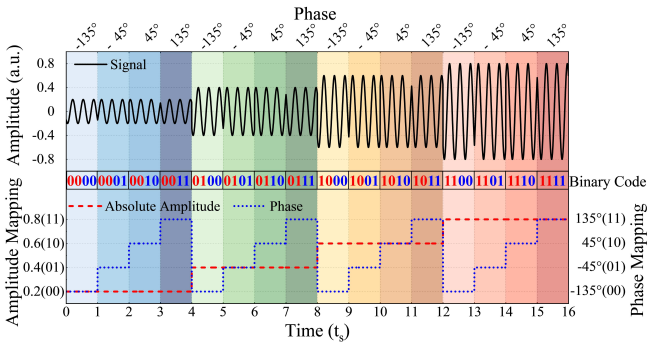


Fig. 2. Mapping of symbol amplitudes and phases to binary codes in the 16APSK scheme. The black curve represents the symbol waveform, the red dashed line indicates the amplitude mapping of the binary code, and the blue dotted line denotes the phase mapping of the binary code.

The modulation signal can be described as $m(t) = A_{\rm m}\cos(\omega_{\rm m}t + \varphi_{\rm m})$, where $A_{\rm m}$, $\omega_{\rm m}$, and $\varphi_{\rm m}$ are the amplitude, angular frequency, and phase, respectively. The microwave electric field strength is given by $E_{\rm MW} = E_0(1 + \kappa m(t)/A_{\rm m})\cos(\omega_{\rm c}t + \varphi_{\rm c})$, where κ is the modulation depth, and E_0, $\omega_{\rm c}$, and $\varphi_{\rm c}$ are the carrier amplitude, angular frequency, and phase, respectively. Based on the rotating-wave approximation and the atomic relaxation time, the high-frequency carrier $\omega_{\rm c}$ is filtered out, yielding the effective Rabi frequency $\Omega_{\rm MW,eff}(t) \approx \Omega_0(1 + \kappa m(t)/A_{\rm m})/\sqrt{2}$, where $\Omega_0 = \mu_{34}E_0/\hbar$. The self-demodulation principle arises from the fractional nonlinear response of the atomic system: the density matrix element ρ_{21} depends on $\Omega_{\rm MW}^2$, leading to a susceptibility χ_{21} that varies with $m(t)$. The probe laser transmission signal $S(t) \propto {\rm Im}[\chi_{21}(t)]$ directly reflects $m(t)$, eliminating the need for an external mixer.

The core of APSK resides in the mapping of amplitude and phase, which determines how data bits are encoded onto the signal. Figure 2 illustrates the encoding mapping of the 16APSK scheme, where symbol amplitude and phase each carry two bits of binary information, with the symbol duration set to three units. The black curve depicts the symbol waveform, while the binary code axis lists the corresponding binary codes, with the first two bits representing the symbol's amplitude information and the last two bits representing its phase information. The red dashed line indicates the mapping between the absolute amplitude of the symbol and the corresponding binary code combination, while the blue dotted line represents the phase mapping. The information density can be improved by mapping information into multiple dimensions of the signal

through the APSK method. The RAR enables the direct recovery of amplitude and phase without down-conversion and filtering.

3. Results and discussion

To validate the feasibility of the APSK scheme, a pseudo-random bit sequence was practically transmitted. Figure 3(a) illustrates the complete signal encoded in the 16APSK scheme, with each symbol having a duration of three units. The gray curve represents the original signal directly output from the AFG, while the red curve depicts the received signal obtained through self-demodulation by the RAR. The signal after self-demodulation can be directly utilized for decoding. By segmenting the signal into individual symbols according to the symbol duration and applying the mapping relationship shown in Fig. 2, the corresponding binary codes can be obtained. Subsequent reassembly enables the reconstruction of the original bit sequence. During the decoding process, predefined tolerance intervals are established to ensure robust performance. These intervals are specifically configured as half the interval on either side of the mapped amplitude and phase values of distinct symbols. While a slight discrepancy between the received and transmitted signals may occasionally be observed, such as at the "0010" binary code in the zoomed-in views in Fig. 3(b), this deviation is within the tolerance range and does not influence the decoding process. As a result, overall signal shifts or minor amplitude jitter do not influence the accuracy of signal recovery and recognition. Precise segmentation of the symbol data and accurate identification of the amplitude and phase of each segment enable reliable reconstruction of the original bit sequence.

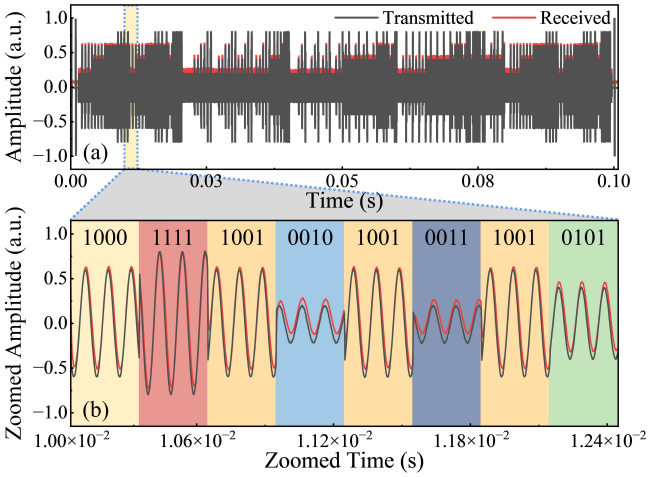


Fig. 3. (a) Transmitted and received APSK signals in the time domain. (b) Zoomed-in view of multiple APSK symbols. The gray curve (Transmitted) represents the APSK signal, while the red curve (Received) depicts the signal demodulated by the RAR.

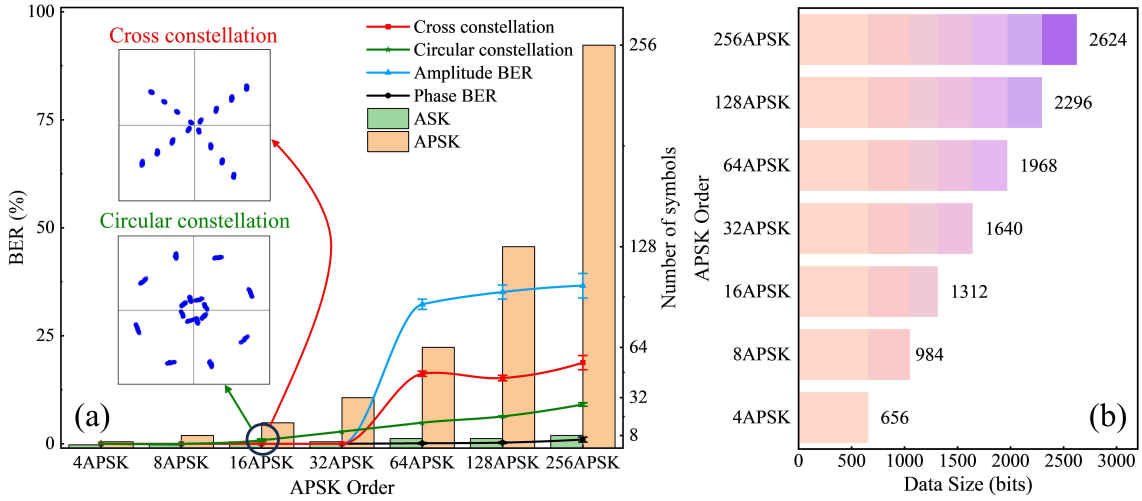


Fig. 4. (a) Evaluation of the BER and the number of symbols for APSK signals of different orders. The blue, black, and red curves represent the amplitude BER, phase BER, and total BER for the cross constellation, respectively. The green curve represents the BER for the circular constellation. The cross and circular constellations are shown for 16APSK. The green bar represents the number of symbols for conventional ASK, while the yellow bar represents that for the APSK signal. (b) Transmitted data size of the APSK signal under different encoding orders.

The relationship between BER trends across different APSK encoding orders and the number of symbols is illustrated in Fig. 4(a). The cross constellation allows for a more intuitive observation of the RAR's response to amplitude and phase variations. The blue, black, and red curves in Fig. 4(a) represent the amplitude, phase, and total BER of the cross constellation, respectively. The BER curves reveal that a low BER is maintained for 32APSK. However, when the encoding order reaches 64APSK, the amplitude levels are doubled from four to eight within the available range, causing a significant increase in symbol misjudgment and a sharp rise in BER. In contrast, a relatively low phase BER is maintained even at 256APSK, demonstrating stability in phase encoding. This phase stability allows for further increases in information capacity by extending the number of phase levels. Additionally, the green curve in Fig. 4(a) employs the constellation mapping from the DVB-S2X standard. This circular constellation utilizes fewer amplitude levels, resulting in

a consistently low and stable overall BER. Figure 4(a) also presents the cross and circular constellations for 16APSK, allowing for a direct visual observation that the circular constellation possesses fewer amplitude levels. Furthermore, the bar chart shows an exponential increase in the number of available symbols for the cross constellation across orders ranging from 4APSK to 256APSK. Compared to conventional ASK, which relies solely on amplitude, the number of definable symbols in APSK is significantly increased by incorporating the phase dimension. This exponential growth in the symbol set size directly correlates with a substantial enhancement in information capacity and data transmission capability.

To ensure consistency in the number of symbols across APSK signals with different encoding orders during BER evaluation, while mitigating variations in data content arising from differing data volumes, De Bruijn sequences are utilized to standardize the overlapping data segments. Specifically, a master binary sequence is first constructed based on a linear De Bruijn sequence $B(k,n)$, with a binary alphabet size $k=2$ and a subsequence length $n=8$ (corresponding to the highest modulation order, 256APSK). This sequence guarantees full coverage of all possible 8-bit patterns and exhibits excellent pseudorandom properties. The master sequence is then formed by repeating this base De Bruijn sequence sufficiently many times. For each APSK order with a bit length of m (m ranging from 2 to 8), the data sequence is obtained by truncating a prefix of length $N\times m$ from the same master sequence, where N represents the constant number of symbols maintained across all orders. This construction ensures that the BER evaluation is not influenced by the inherent characteristics of the data content, thereby facilitating a fair comparison. The data sizes for different encoding orders employed in the BER assessment are illustrated in Fig. 4(b), where the bit sequences in segments of the same color are identical. The symbol distribution in bit sequences across various APSK orders remains consistently close to uniform. This is maintained even for the 256APSK sequence, where all symbols are guaranteed to appear, thereby minimizing deviations due to uneven distribution and ensuring a fair and reliable evaluation.

A 33×33 pixel QR code image was transmitted to demonstrate the practical performance of the APSK signal and compare the impact of varying symbol durations on BER. The original image was converted into an 8712-bit binary sequence and encoded as a 16APSK signal with varying symbol durations for transmission. Figure 5 presents the original image alongside the recovery results for different symbol durations. The reconstructed image with one-unit symbol duration (Fig. 5(b)) exhibits significant noise and distortion, with limited QR code readability compared to the original (Fig. 5(a)). When increased to two-unit symbol duration, the reconstructed image (Fig. 5(c)) shows reduced noise and minor pixel errors. As the symbol duration increases to three units, the reconstructed image (Fig. 5(d)) is identical to the original image (Fig. 5(a)). For the one-unit symbol duration APSK signal, 678 error bits were observed, resulting in a BER point estimate of 7.78×10^{-2}. Using the Clopper–Pearson method, the two-sided 95% confidence interval is $[7.24\times 10^{-2},\ 8.36\times 10^{-2}]$. For the two-unit symbol duration APSK signal, 515 error bits were detected in the decoded bit sequence, yielding a BER point estimate of 5.91×10^{-2}, with a 95% confidence interval of $[5.44\times 10^{-2},\ 6.42\times 10^{-2}]$. For the three-unit symbol duration APSK signal, no errors were observed in the decoded bit sequence, and the BER point estimate is 0. The two-sided 95% confidence interval is $[0,\ 4.23\times 10^{-4}]$, and with a one-sided 95% confidence upper limit, the true BER is estimated to be less than 3.44×10^{-4} with 95% confidence. The frequency of the APSK signals was fixed at 10 kHz for all symbol durations. Specifically, the one-unit symbol duration corresponds to a single carrier period (100 μs), resulting in a symbol rate of 10 kBd and a bit rate of 40 kbps (4 bits/symbol). Similarly, the durations for two-unit and three-unit symbols correspond to symbol rates of 5 kBd (20 kbps) and 3.33 kBd (13.33 kbps), respectively. The relatively high BER (7.78×10^{-2}) observed at 10 kBd (one-unit) suggests that the system operates near the limit of its instantaneous bandwidth, where the atomic response fails to fully track rapid symbol transitions. Conversely, reducing the rate to 3.33 kBd (three-unit) effectively mitigates these bandwidth constraints, enabling error-free transmission. This confirms that while higher transmission rates are achievable, maximizing reliability for complex data, such as images, necessitates optimizing the symbol duration within the response envelope of the receiver.



Fig. 5. Performance of APSK signals with different symbol durations for QR code transmission. (a) Original image. (b) Reconstructed image with one-unit symbol duration. (c) Reconstructed image with two-unit symbol duration. (d) Reconstructed image with three-unit symbol duration.

4. Conclusion

This work introduces an APSK method for digital signal transmission in wireless communication based on RAR. By applying programmed encoding of the amplitude and phase of sine signals, the introduction of phase information into AM signals significantly expands the information capacity of amplitude-modulated digital signals. Experimental results demonstrate that APSK substantially outperforms conventional ASK systems in terms of information capacity. The 16APSK scheme generates 16 distinct amplitude-phase states, whereas traditional ASK with equivalent 2-bit amplitude encoding provides only 4 states, increasing the bits per symbol from 2 to 4 and thereby doubling the information capacity. Importantly, this exponential growth in information capacity does not compromise signal reliability. Under optimized encoding orders such as 16APSK and 32APSK, the system maintains zero bit errors. To further validate the practical application potential of the APSK system, an image transmission experiment was conducted. The reconstructed image at three-unit symbol duration achieves lossless reconstruction of the original, while shorter durations introduce increasing noise, with BER values of 7.78×10^{-2}, 5.91×10^{-2}, and 0 for one-, two-, and three-unit durations, respectively. This indicates that extending symbol duration enhances reliability. This work supplements research on APSK in microwave signal modulation techniques employing RAR, providing references for advancing quantum communication. The potential of the APSK system extends beyond fixed constellation patterns. A pivotal direction for future research is the geometric shaping of constellations tailored to specific channel characteristics. The circular structure of APSK offers greater flexibility to mitigate nonlinear distortion and phase noise inherent in the Rydberg atomic receiver system. By dynamically optimizing the amplitude ratios and phase differences based on real-time channel conditions, there is significant room for further reduction in BER. Consequently, future work will focus on adaptive constellation design to maximize both spectral efficiency and robustness in complex electromagnetic environments.

Acknowledgments

Project supported by the Quantum Science and Technology-National Science and Technology Major Project (Grant No. 2023ZD0300902), the National Natural Science Foundation of China (Grant Nos. 12474359 and 62475136), the Fundamental Research Program of Shanxi Province (Grant No. 202403021211158), the Fund Program for the Scientific Activities of Selected Returned Overseas Professionals in Shanxi Province (Grant No. 2023001), the Shanxi Scholarship Council of China (Grant No. 2024-003), and the Fund for Shanxi "1331 Project".

References

[1] Schlossberger N, Prajapati N, Berweger S, Rotunno A P, Artusio-Glimpse A B, Simons M T, Sheikh A A, Norrgard E B, Eckel S P and Holloway C L 2024 *Nat. Rev. Phys.* **6** 606
[2] Yuan J, Yang W, Jing M, Zhang H, Jiao Y, Li W, Zhang L, Xiao L and Jia S 2023 *Rep. Prog. Phys.* **86** 106001
[3] Zhang H, Ma Y, Liao K, Yang W, Liu Z, Ding D, Yan H, Li W and Zhang L 2024 *Sci. Bull.* **69** 1515
[4] Wu B, Yao J W, Wu F C, An Q and Fu Y Q 2024 *Chin. Phys. B* **33** 024205
[5] Liu B, Zhang L H, Wang Q F, Ma Y, Han T Y, Liu Z K, Zhang Z Y, Shao S Y, Zhang J, Li Q, Chen H C, Han Y L, Ding D S and Shi B S 2025 *Chin. Phys. Lett.* **42** 053201
[6] Gong T, Chandra A, Yuen C, Guan Y L, Dumke R, See C M S, Debbah M and Hanzo L 2025 *IEEE Wirel. Commun.* **32** 90
[7] Gordon J A, Holloway C L, Schwarzkopf A, Anderson D A, Miller S, Thaicharoen N and Raithel G 2014 *Appl. Phys. Lett.* **105** 24104
[8] Liu Z K, Zhang L H, Liu B, Zhang Z Y, Guo G C, Ding D S and Shi B S 2022 *Nat. Commun.* **13** 1997
[9] Song Z, Liu H, Liu X, Zhang W, Zou H, Zhang J and Qu J 2019 *Opt. Express* **27** 8848
[10] Otto J S, Hunter M K, Kjærgaard N and Deb A B 2021 *J. Appl. Phys.* **129** 154503
[11] Yuan S S A, Xu X Y I, Yuan J, Xie G, Huang C, Chen X, Huang Z and Sha W E I 2025 *IEEE Antennas Wirel. Propag. Lett.* **24** 1839
[12] She Z, Zhu X, Lin Y, Li X, Yang X, Shang Y, Teng Y, Tu H, Liao K, Zhang C, Liu X, Chen J and Huang W 2024 *Chin. Phys. Lett.* **41** 84201
[13] Cui M, Zeng Q and Huang K 2024 *IEEE Commun. Mag.* **64** 146
[14] Prajapati N, Rotunno A P, Berweger S, Simons M T, Artusio-Glimpse A B, Voran S D and Holloway C L 2022 *AVS Quantum Sci.* **4** 035001
[15] Wu H, Yao X, Xie C, Wu K D, Wu S, Ni R, Xiang G Y and Gong C 2025 *IEEE Trans. Commun.* **73** 6440
[16] Wang H, Boone C T and Iyanu G H 2025 *Quantum Sensing, Imaging, and Precision Metrology III*, January 25–31, 2025, San Francisco, California, USA, pp. 239
[17] Xie Y, Lei M, Xing Z, Zhang J, Dong W and Shi M 2025 *J. Appl. Phys.* **138** 114401
[18] Li H, Hu J, Bai J, Shi M, Jiao Y, Zhao J and Jia S 2022 *Opt. Express* **30** 13522
[19] Yuan J, Jin T, Xiao L, Jia S and Wang L 2023 *IEEE Antennas Wirel. Propag. Lett.* **22** 2580
[20] Xu X Y I, Xie G, Ma J, Ying L, Yuan J, Huang Z and Sha W E I 2024 *Opt. Express* **32** 21755
[21] Liu X B, Jia F D, Zhang H Y, Mei J, Liang W C, Zhou F, Yu Y H, Liu Y, Zhang J, Xie F and Zhong Z P 2022 *Chin. Phys. B* **31** 090703
[22] Meyer D H, Cox K C, Fatemi F K and Kunz P D 2018 *Appl. Phys. Lett.* **112** 211108
[23] Zhang P, Yuan S, Jing M, Yuan J, Zhang H and Zhang L 2024 *IEEE Photonics J.* **16** 3000307
[24] Li D, Bai Z, Zuo X, Wu Y, Sheng J and Wu H 2024 *Appl. Phys. Rev.* **11** 41420
[25] Wu H, Wu S, Gong C, Li S, Ni R and Zhu J 2024 *Proc. CSNDSP* pp. 74
[26] Wu Y, Xiao D, Zhang H and Yan S 2025 *Chin. Phys. B* **34** 013201
[27] Holloway C L, Simons M, Haddab A H, Gordon J A, Anderson D A, Raithel G and Voran S 2021 *IEEE Antennas Propag. Mag.* **63** 63
[28] Anderson D A, Sapiro R E and Raithel G 2021 *IEEE Trans. Antennas Propag.* **69** 2455
[29] Wen W, Yan S, Wang R, Li X, Tan J, Pang X, Zhai W, Cui W and Gao Y 2024 *Opt. Express* **32** 42872
[30] Cai Y, Shi S, Zhou Y, Li Y, Yu J, Li W and Li L 2023 *Phys. Rev. Appl.* **19** 044079
[31] Anderson D A, Sapiro R E and Raithel G 2020 *IEEE Aerosp. Electron. Syst. Mag.* **35** 48
[32] Djordjevic I B, Xu L and Wang T 2011 *IEEE Photonics J.* **3** 1030
[33] Razaul Md, Mushfiq S and Asif Md 2017 *Int. J. Comput. Appl.* **161** 30
[34] Yuan S S A, He Z, Chen X, Huang C and Sha W E I 2022 *IEEE Antennas Wirel. Propag. Lett.* **21** 446
[35] Holloway C L, Simons M T, Gordon J A and Novotny D 2019 *IEEE Antennas Wirel. Propag. Lett.* **18** 1853
[36] Thomas C, Weidner M and Durrani S 1974 *IEEE Trans. Commun.* **22** 168
[37] Taga H, Wu J Y, Shih W T and Shu S S 2008 *Opt. Express* **16** 384
[38] Zhao L 2024 *Appl. Comput. Eng.* **36** 53
[39] Sung W, Kang S, Kim P, Chang D and Shin D 2009 *Int. J. Satell. Commun. Netw.* **27** 295
[40] De Gaudenzi R, Guillen I Fabregas A and Martinez A 2006 *IEEE Trans. Wirel. Commun.* **5** 2396